








Exchange spin waves in thin films with gradient composition

I. A. Golovchanskiy ^{1,2,3,*} I. V. Yanilkin ^{4,5} A. I. Gumarov ^{4,5} B. F. Gabbasov ^{4,5} N. N. Abramov,²
R. V. Yusupov ⁴ R. I. Khaibullin ⁵ and L. R. Tagirov ^{4,5,†}¹Moscow Institute of Physics and Technology, National Research University, 9 Institutskiy per., Dolgoprudny, Moscow Region 141700, Russia²National University of Science and Technology MISIS, 4 Leninsky prosp., Moscow 119049, Russia³Dukhov Research Institute of Automatics (VNIIA), 127055 Moscow, Russia⁴Institute of Physics, Kazan Federal University, Kremlyovskaya str. 18, 420008 Kazan, Russia⁵Zavoisky Physical-Technical Institute, FRC Kazan Scientific Centre of RAS, 420029 Kazan, Russia

(Received 6 April 2022; revised 12 May 2022; accepted 26 May 2022; published 7 June 2022)

We report on an investigation of magnetic resonance phenomenon in ferromagnetic thin films with controlled nonuniform composition. An epitaxial Pd-Fe thin film with linear distribution of Fe content across the thickness is used as the model material. Anomalous perpendicular standing spin waves are observed and quantified using the collective dynamic equation. Numerical analysis yields the exchange stiffness constant for the diluted Pd-Fe alloy $D = 2A/\mu_0 M_s = 15 \text{ T} \cdot \text{nm}^2$ and the ratio of the effective magnetization to the saturation magnetization $M_{\text{eff}}/M_s = 1.16$. It is demonstrated that, overall, the engineering of thin films with nonuniform composition across the thickness can be used for high-frequency or low-field magnonic operations using exchange spin waves.

DOI: [10.1103/PhysRevMaterials.6.064406](https://doi.org/10.1103/PhysRevMaterials.6.064406)

I. INTRODUCTION

Magnonics is an expanding field of research that offers approaches for the transmission and processing of microwave signals via spin waves (i.e., magnons) [1–8]. Practical advantages of the magnonics include tunability of the magnon frequencies via the external field, material choice, or the geometry of the magnon media, charge-current-free nature and low power consumption of the spin-wave transfer, and micro- and sub-micro-scales of spin waves at microwave frequencies, which allows to target the creation of microdevices for the processing of microwave information. Currently, the applied magnonics is progressed towards the development of magnon logic devices [7], i.e., waveguides [9], magnon transistors [10], directional couplers [11], majority gates [12,13], non-Boolean devices [5], and neuromorphic circuits [14,15]. Also, magnonics finds its application in spintronic systems [4,16–19]. Precessing magnetization is used as the source of the spin current in a conductor that is induced by the spin pumping at the interface of the ferromagnet/conductor bilayer. The charge current is subsequently converted from the spin current via the inverse spin-Hall effect in the adjacent conductor. As an alternative direction of research, cavity magnonics [20–26] aims at the single quantum operations and considers hybridization of magnons with photons. Cavity magnonics offers various promising technologies, including hybrid quantum platforms [27,28], magnon memory [29], and microwave-to-optical quantum transducers [30].

Arguably, one of the most desired characteristics, regardless of the particular application, is high magnon frequency at zero or low magnetic fields. Quite a number of approaches were proposed in recent years that allowed to achieve high

frequencies at low fields. For instance, the enhanced eigenfrequencies of a thin-film magnonic media can be accessed by engineering the magnetic anisotropy at interfaces of thin-film heterostructures [31–34] by considering antiferromagnetic exchange interactions [19,35–37], or using mechanisms of hybridization with superconducting structures [38–40].

Technically, high eigenfrequencies in the magnonic media at low magnetic fields can be reached much more easily by exploiting exchange spin waves. Indeed, for perpendicular standing spin waves in ferromagnetic films [41–43] the effective exchange field H_{ex} scales with the thickness d as $H_{\text{ex}} = (2A/\mu_0 M_s)k^2$, where A is the exchange stiffness constant, M_s is the saturation magnetization, $k = 2\pi n/d$ is the wave vector, and n is the mode number. An appropriate choice of ferromagnetic material or of just the film thickness allows to achieve eigenfrequencies in the range from GHz up to sub-THz. However, conventionally, coupling of perpendicular exchange spin waves in thin films with microwave fields requires fixed spin boundary conditions at least at one of the film surfaces. Otherwise, the dynamics susceptibility of the perpendicular spin waves is zero.

Often spin-wave boundary conditions in ferromagnetic films are free and the operation with the exchange spin waves requires more sophisticated approaches. For instance, as demonstrated recently, the excitation of exchange spin waves can be achieved using the dipole or the interface exchange interactions in magnon-magnon hybrid structures [44–48] or by employing spin transfer torque nanooscillators [49–51]. More exotic approaches for the excitation of exchange spin waves include the employment of moving superconducting vortex lattice [52] or resonating skyrmions [53]. As a drawback, these approaches are hardly flexible in terms of selection of materials and conditions for spin-wave excitation.

In this work, we propose and explore a more traditional approach for the excitation of exchange spin waves and tuning

*golov4anskiy@gmail.com

†ltagirov@mail.ru

of the effective exchange energy. We study exchange spin waves in thin films with nonuniform composition across the thickness. As was reported earlier [54–59], the spectrum of perpendicular exchange spin waves in thin films with nonuniform composition across the thickness acquires a dependence on the particular distribution of magnetic parameters across the thickness of the film, making the spectrum anomalous; the spin-wave eigenvalue problem is reduced to the Schrödinger equation. In addition, nonuniform composition ensures the nonzero dynamic susceptibility of perpendicular spin waves regardless of boundary conditions. With the modern development of thin-film deposition techniques, opportunities for the fabrication of thin films with predefined distribution of ferromagnetic parameters across the thickness are vast.

We perform our proof-of-principle measurements on an epitaxially grown Pd-Fe alloy thin film as the model material. The dilute Pd-Fe alloys belong to a class of ferromagnets composed of palladium or platinum doped with transition metals (i.e., Fe, Co, and Ni). A low concentration of transition metals induces spontaneous magnetization of alloys with several K Curie temperature and with a “giant” effective magnetic moment per magnetic atom [60]. Such diluted alloys are of particular interest in superconducting spintronics [61–68]. For higher concentrations, the magnetization and the Curie temperature increase approximately linearly with increasing Fe concentration up to 400 K for 20 at.% of Fe [66,69]. At last, strong ferromagnetic superstructured Fe-Pd, Fe-Pt, Co-Pt films with equiatomic composition are characterized by large magnetocrystalline anisotropies [70,71] and find its application in hard-drives [72], micro-devices [73,74], and high-frequency ferromagnetic resonance applications [75,76]. The spin-wave dynamics studied in this work contributes to the understanding of magnetic phenomena in the Pd-Fe system, as well as enriches the range of potential applications of Pd-Fe alloys.

II. EXPERIMENTAL DETAILS

The epitaxial Pd-Fe film samples with gradient composition across their thickness were fabricated by molecular-beam epitaxy (MBE) in ultrahigh vacuum conditions of 5×10^{-10} mbar (SPECS Surface Nano Analysis GmbH). Epitaxial (100)-MgO single-crystal substrates were used with dimensions of $5 \times 10 \times 0.5$ mm³ provided by Crystal GmbH. Iron and palladium were evaporated simultaneously from CreaTec Fischer effusion cells with precise temperature control of $\pm 0.1^\circ$ C. During the deposition process, the temperature of the palladium was constant, while the temperature of the iron was varied over time to obtain a desired profile of Fe content across the thickness of synthesized films. The film growth was carried out in two stages, in analogy with Ref. [77]. Details of the procedure can be found in [78]. The structural perfection of the film was monitored *in situ* at each stage by low-energy electron diffraction (LEED) and has shown single-crystallinity of the growing Pd-Fe film.

Next, the synthesized samples were cut into several pieces for further studies. One piece of the each sample was additionally annealed in an ultrahigh vacuum (9×10^{-9} mbar) at a temperature of 600° C for 2 hours to confirm the stability of

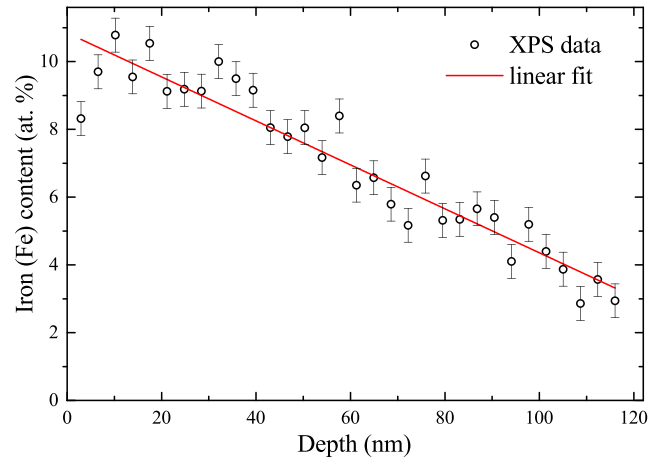


FIG. 1. Iron content across the thickness of the studied Pd-Fe film. Red line shows the linear fit.

the samples: the structural and magnetic properties of samples did not change noticeably after the annealing.

The crystal structure was studied using the Bruker D8 Advance x-ray diffractometer. X-ray diffraction (XRD) studies confirmed the epitaxial growth of a Pd-Fe film on the MgO single-crystal substrate in the “cube-on-cube” mode. More details on the structure and technology of the studied films are provided in [78].

In this work, as the representative example, we focus on the Pd-Fe sample with thickness $d = 116$ nm, in which the concentration of Fe is varied linearly from 3.3 at.% at the interface with the substrate to 10.8 at.% at the free surface (see Fig. 1). The distribution of Fe atomic content across the thickness was verified with x-ray photoelectron spectroscopy (XPS by SPECS) in combination with sequential Ar-ion etching of the sample surface. In [78] we also provided data for an evidence Pd-Fe film with 7 at.% of Fe, uniform distribution of Fe, and thickness 80 nm.

Magnetization measurements were performed using the vibrating-sample magnetometer (VSM) of the QUANTUM DESIGN PPMS-9 setup. The external magnetic field was applied both parallel to the film plane (in-plane) along [100] and [110] crystallographic directions of the cubic MgO single-crystal, and perpendicular (out-of-plane) to the film plane, along the [001] direction. Magnetization measurements reveal an onset of a spontaneous magnetization at about $T = 250$ K for the selected Pd-Fe sample.

Ferromagnetic resonance spectroscopy (referred to as FMR) was performed using the VNA-FMR flip-chip approach [79,80]. The Pd-Fe sample was glued on top of the transmission line of the 50-Ohm-impedance coplanar waveguide equipped with SMP rf connectors and was placed in a homemade superconducting solenoid inside a closed-cycle cryostat (Oxford Instruments Triton, base temperature 1.2 K). The magnetic field was applied out-of-plane, perpendicular to the surface of the waveguide and of the studied Pd-Fe sample (i.e., along the [001] direction). The response of the samples was studied by analyzing the transmitted microwave signal $S_{21}(f, H)$ with the VNA Rohde & Schwarz ZVB20.

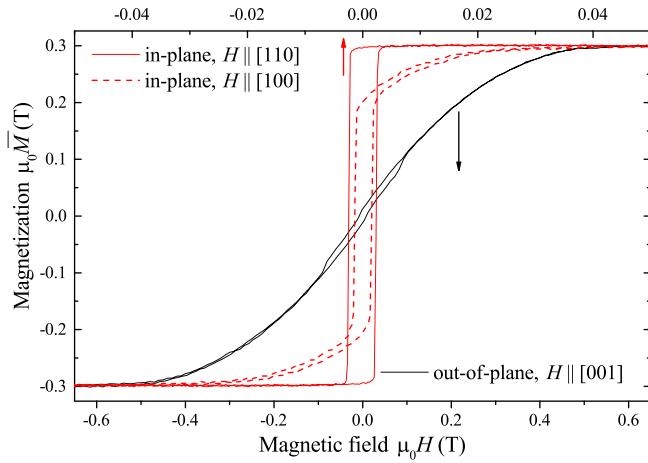


FIG. 2. The dependence of magnetization of the studied Pd-Fe sample on the magnetic field in both the in-plane (red curves, upper x -scale) and the out-of-plane (black curve, lower x -scale) measurement geometries at $T = 5$ K.

Cavity magnetic resonance (CMR) spectroscopy was performed using a commercial X-band Bruker ESP300 electron spin resonance spectrometer equipped with the Oxford Instruments ESR-9 helium flow cryostat. The standard ER4102ST rectangular TE102-mode cavity was used in the measurements. See [81] for more details on the measurement setup and its application for studies of Pd-Fe films.

III. EXPERIMENTAL RESULTS AND DISCUSSION

A. Magnetic properties of Pd-Fe epitaxial films with gradient composition

Figure 2 shows the dependence of magnetization of the Pd-Fe sample on magnetic field at $T = 5$ K for both the in-plane (red curve) and the out-of-plane (black curve) orientations of the magnetic field. All curves indicate a minor hysteresis with the coercive field of several mT, and the volume-averaged saturation magnetization of the Pd-Fe sample about $\mu_0 \bar{M}_s = 0.3$ T. The difference in saturation fields for the in-plane magnetization curves indicates the [110] crystal axis as the easy magnetization direction. The saturation field for the out-of-plane geometry H_s corresponds to some overall effective magnetization $\mu_0 H_s = \mu_0 \bar{M}_{\text{eff}} \approx 0.47$ T, which incorporates the saturation magnetization as well as the averaged uniaxial and cubic anisotropies [33,43].

Figure 3 shows the differentiated FMR spectrum dS_{21}/dH of the same Pd-Fe sample measured at out-of-plane magnetic field and temperature $T = 5$ K. The spectrum reveals three absorption lines indicated with numbers $n = 1, 2, 3$. The line $n = 1$ shows the highest absorption amplitude, though, low FMR signal amplitudes do not allow to estimate relative intensities of spectral lines. The dependence of the FMR frequency on the magnetic field shows linear dependence at $\mu_0 H \gtrsim 0.5$ T following the typical FMR relation for saturated thin films at out-of-plane magnetic fields. At $\mu_0 H \lesssim 0.5$ T the magnetization of the Pd-Fe film starts to relax and the FMR lines deviate from the linear behavior.

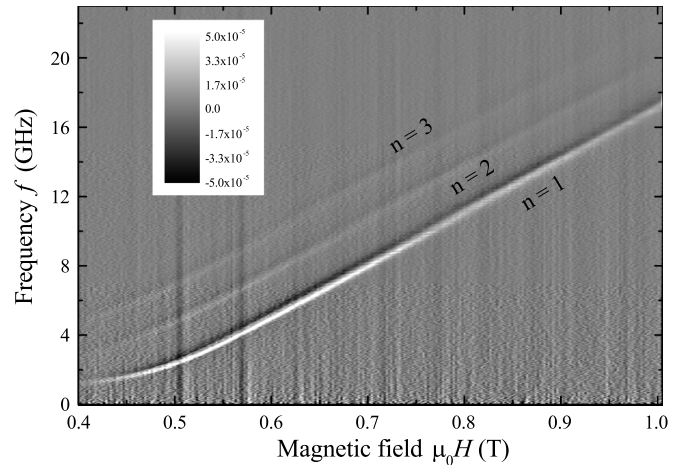


FIG. 3. Differentiated FMR absorption spectrum $dS_{21}(f, H)/dH$ of the Pd-Fe sample at $T = 5$ K.

Relative intensities of resonance lines are obtained by measuring the cavity resonance spectrum. Figure 4 shows the CMR spectrum of the same Pd-Fe sample at the out-of-plane magnetic field at temperature $T = 5$ K and cavity frequency 9.44 GHz. The spectrum reveals five resonance fields indicated with the numbers $n = 1, \dots, 5$. Intensities of the resonances gradually reduce with increasing the mode number.

Figure 5 summarizes ferromagnetic resonance measurements. The symbols in Fig. 5 show experimental FMR and CMR $f_r(H)$ dependencies. In general, the FMR in thin films at the out-of-plane magnetic field above the saturation field obey the modified Kittel formula [41–43]

$$2\pi f_r / \mu_0 \gamma = H + H_{\text{ex}} - M_{\text{eff}}, \quad (1)$$

where γ is the gyromagnetic ratio of Pd-Fe and H_{ex} is the effective exchange field. Fitting the FMR lines at $\mu_0 H > 0.5$ T yields the gyromagnetic ratio $\gamma/2\pi = 30.4$ GHz/T and the effective field term $\mu_0(M_{\text{eff}} - H_{\text{ex}}) = 0.43$ T for $n = 1$, while CMR $n = 1$ resonance field yields $\mu_0(M_{\text{eff}} - H_{\text{ex}}) = 0.46$ T. The gyromagnetic ratio of the Pd-Fe sample is close to the ratio for free electrons 28 GHz/T. Its slightly higher value can

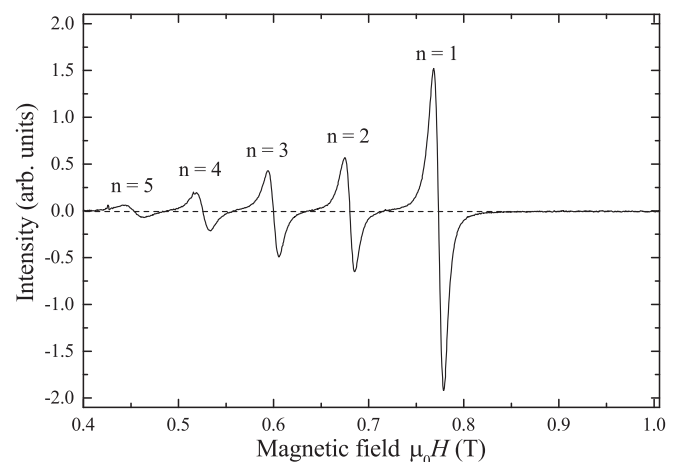


FIG. 4. CMR spectrum of the Pd-Fe sample at $T = 5$ K.

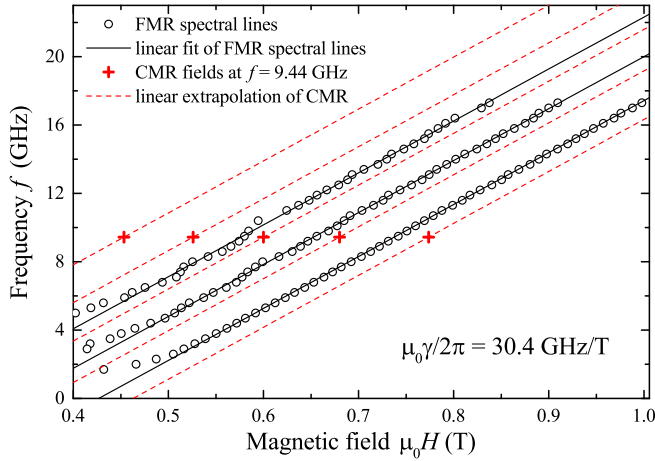


FIG. 5. Experimental $f_r(H)$ dependencies acquired from the FMR spectrum (Fig. 3) are shown with black circles. Black solid lines show the fit of FMR $f_r(H)$ lines with Eq. (1). Resonance fields obtained by the CMR measurements at $f_r = 9.44$ GHz (Fig. 4) are shown with red crosses. Red dashed lines show extrapolation of CMR using Eq. (1) and the gyromagnetic ratio obtained from the FMR lines.

be explained within the two sublattice model [82,83] by larger g -factor for Pd than for Fe.

The obvious shift between CMR and FMR resonances in Fig. 5 by $\mu_0 H = 0.03$ T indicates the presence of an additional exchange field in the case of FMR measurements. We state that this exchange field appears due to the ferromagnetic skin effect [84–86]. At certain conditions, in the case of asymmetric excitation of magnetization dynamics, as done by the coplanar waveguide in FMR measurements, microwave currents induced in conducting ferromagnetic films partially screen external microwave fields. This localized screening enables the excitation of magnetization dynamics with nonzero wave vector, which contributes to the process by an additional exchange field and shifts the resonance frequency as compared to the Kittel mode. In the case of the CMR measurements the excitation microwave fields are applied symmetrically at both surfaces of the film and the localized screening process does not enable an additional exchange field. Below we focus on CMR data for simplicity.

B. Exchange spin waves in Pd-Fe epitaxial films with gradient composition

Resonance modes $n = 1, \dots, 5$ in Figs. 3–5 are referred to as the perpendicular standing spin wave (PSSW) resonances [41–43] where the nonzero spin wave vector induces an effective exchange field. Figure 6(a) shows the dependence of the CMR resonance field on the mode number $H_r(n)$, Figure 6(b) shows the dependence of the relative CMR amplitude on the mode number $I(n)$. For the conventional exchange PSSW the dependence $H_r(n)$ is parabolic due to the k^2 factor of the H_{ex} in Eq. (1). In contrast, the dependence $H_r(n)$ in Fig. 6(a) is approximately linear, which indicates that the spin wave resonances can be characterized as anomalous [54–56]. Anomalous spin wave resonances appear when any magnetic property, i.e., the saturation magnetization, magnetic anisotropies, or the exchange stiffness, is nonuniform across the thickness of the ferromagnetic film. In our case, all three parameters are nonuniform due to the gradient composition of the Pd-Fe film.

PSSW in ferromagnetic films can be treated comprehensively by means of the collective dynamic equation [54–59]. It can be shown that, by starting from the Landau–Lifshitz equation for an individual layer inside the film coupled to neighboring layers via the exchange interaction, the dynamic equation is derived in the form of the Schrödinger equation

$$\left[-D(z) \frac{\partial^2}{\partial z^2} + V(z) \right] m(z) = \frac{2\pi f_r}{\gamma} m(z), \quad (2)$$

where $m(z)$ is the dependence of the locally normalized amplitude of the magnetization precession across the thickness of the film, $D(z) = 2A(z)/\mu_0 M_s(z)$ is the normalized exchange stiffness coefficient, and $V(z) = H - M_{eff}(z) + D(z)/M_s(z) \frac{\partial^2}{\partial z^2} M_s(z)$ is the potential well. The general boundary conditions of the eigenvalue problem in Eq. (2) are [57,87–89]

$$dm/dz + \alpha_s m = 0, \quad (3)$$

where $\alpha_s = K_s/A_s$ is the surface coefficient, K_s is the surface anisotropy, and A_s is the exchange stiffness constant at the surface. In the case of $\alpha_s = 0$ the spin boundary conditions are free. In the case of $1/\alpha_s = 0$ the spin boundary conditions are fixed or pinned.

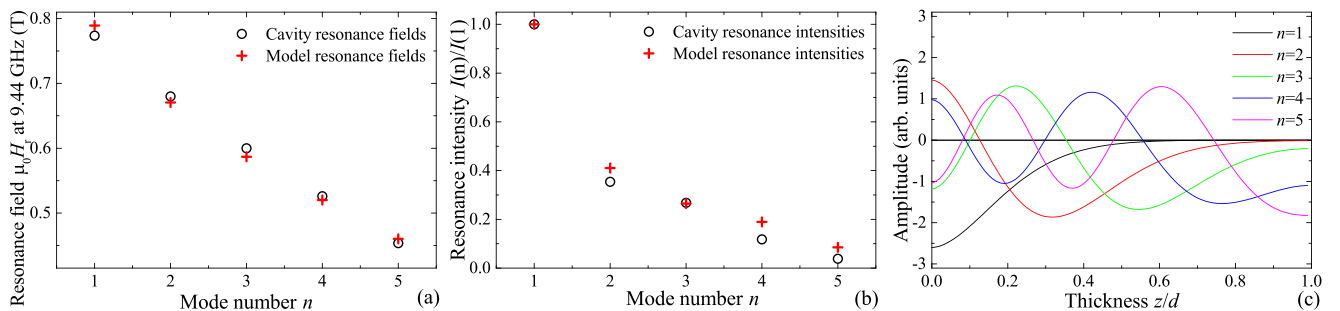


FIG. 6. (a) Dependencies of resonance fields on the mode number $\mu_0 H_r(n)$ at $f = 9.44$ GHz. (b) Normalized dependencies of resonance intensities on the mode numbers $I(n)/I(1)$. (c) Dependencies of amplitudes of magnetization precession across the thickness of the film for different modes n .

The intensity of the resonance can be derived with the following expression:

$$I \propto \int h_{rf}(z)m(z)M_s(z)dz, \quad (4)$$

where $h_{rf}(z)$ is the distribution of the rf magnetic field inside the film. It should be noted that the proper derivation of $h_{rf}(z)$ would require to account for the so-called ferromagnetic skin effect via the self-consistent analysis of the spin-dynamic Eq. (2) in combination with the Maxwell equations, as was done in [84–86]. Such an analysis is challenging as it would require the dependence of resistivity ρ on Fe content; it is beyond the scope of this work. In this work we treat the ferromagnetic skin effect by defining the distribution of the rf magnetic field as $h_{rf} \propto \cosh[(z-d/2)/\sigma_f]$, where $\sigma_f = \sigma_0(\Delta H/\overline{M}_s)^{1/2}[H_r/(H_r + \overline{M}_s)]^{1/4} \approx 0.1\sigma_0$ is the ferromagnetic skin depth [84–86], $\sigma_0 = \sqrt{\rho/\pi\mu_0 f_r}$ is the conventional electromagnetic skin depth, ΔH is the resonance linewidth, and H_r is the resonance field (see Fig. 4).

CMR resonances are analyzed using Eqs. (2) and (3) as follows. We consider the linear dependence of the concentration of Fe C_{Fe} across the thickness $C_{Fe} = 10.8 - 7.5z/d$ at.%. The local saturation magnetization $M_s(z)$ is found as $C_{Fe} \times \overline{M}_s/7.1$. This value of the specific magnetization per at.% of Fe is consistent with the magnetization of the evidence sample [78]. Next, it is assumed that the local effective magnetization is proportional to the local saturation magnetization $M_{\text{eff}}(z) = \beta_K M_s(z)$, where $\beta_K < 1$ corresponds to the easy out-of-plane anisotropy and vice versa. At last, it can be noted that, due to the linear dependence of both the saturation magnetization and the Curie temperature on Fe composition [66,69], the exchange coefficient D can be considered as independent of the composition and, thus, constant across the thickness of the film.

In numerical calculations we optimize the resonance fields of spin waves [see Fig. 6(a)]. The optimum fit is obtained with $D = 15 \text{ T} \cdot \text{nm}^2$, $\beta_K = 1.16$, and free boundary conditions. The exchange coefficient D is well consistent with typical values for ferromagnetic metals. For instance, in permalloy with $A = 1.2 \times 10^{-11} \text{ J/m}$ and $\mu_0 M_s = 1 \text{ T}$ the exchange coefficient is $D = 30 \text{ T} \cdot \text{nm}^2$. The obtained $\beta_K = 1.16 > 1$ indicates that the hard axis is aligned out-of-plane, which is well consistent with previous studies of epitaxial Pd-Fe films [66] and with the magnetization measurements of the evidence sample [78]. The obtained free boundary conditions are in agreement with our FMR studies of Pd-Fe films with uniform composition [66,78]: for such films we do not observe PSSW resonances. Figure 6(b) shows the dependence of resonance amplitudes on the mode number calculated using Eq. (4) and the optimized ferromagnetic skin depth $\sigma_f = 70 \text{ nm}$. Both the experimental and numerical $I(n)$ decrease progressively with the mode number and show comparable values. The reasonable match between the experimental and theoretical $I(n)$ reflects the action of the ferromagnetic skin effect [84–86]. The ferromagnetic skin depth $\sigma_f = 70 \text{ nm}$ corresponds to the conventional skin depth $\sigma_0 = 0.7 \mu\text{m}$ and to the resistivity $\rho = 2 \mu\Omega\text{cm}$, which is consistent with the values of resistivity in Pd and Pd-Fe alloys [90–92]. Figure 6(c) shows dependencies of the locally normalized amplitude of the magnetization precession on position $m(z)$ for the first five modes.

For demonstration purposes we consider sine and cosine distributions of Fe across the thickness of a 100-nm film: $C_{Fe} = 10 + 8 \sin(2\pi z/d)$ at.%, and $C_{Fe} = 10 + 8 \cos(2\pi z/d)$ at.%, with the same parameters D and β_K as in Fig. 6. For considered compositions the maximum, the minimum, and the average Fe content are identical. Yet the resonance conditions for PSSW in these films are different. For simplicity the rf field h_{rf} in Eq. (4) is taken as constant.

Figure 7 shows resonance fields, intensities, and distributions of amplitudes of magnetization precession for the considered compositions. It is instructive and interesting to interpret magnetization dynamics in such films in terms of magnons, their localization, and mutual interaction. The sine distribution corresponds to the formation of a potential well for magnons at $z/d = 1/4$, a local barrier at $z/d = 3/4$, and, thus, another local well at $z/d = 1$, in accordance with Eq. (2) [see the upper panel in Fig. 7(c)]. The first three magnon modes are localized within the well at $z/d = 1/4$ [see the lower panel in Fig. 7(c)]. The fourth mode corresponds to a magnon, which is localized in vicinity to $z/d = 1$ [the red dashed curve in the lower panel in Fig. 7(c)]. Magnon modes $n = 5$ and $n = 6$ involve magnetization dynamics across the entire film and can be thought of as global. The sine profile results in the monotonous decrease of the resonance field with the mode number [Fig. 7(a)]; the strongest magnon modes are $n = 1$ and $n = 4$ [Fig. 7(b)] that are two local modes at $z/d = 1/4$ and $z/d = 1$, respectively, with the lowest momentum.

The case of cosine distribution is even more curious. In accordance with Eq. (2) the cosine distribution of Fe leads to the formation of two symmetrical identical wells at $z/d = 0$ and $z/d = 1$ [see the upper panel in Fig. 7(d)]. Magnetization dynamics in such a system can be thought of as a result of the magnon-magnon hybridization [44–48] between identical magnons localized at $z/d = 0$ (left) and $z/d = 1$ (right) that form acoustic (symmetric) and optic (antisymmetric) modes. The $n = 1$ mode corresponds to the acoustic hybridization between the lowest-momentum left and right magnons [black solid curve on the lower panel in Fig. 7(d)], while the $n = 2$ mode corresponds to the optic hybridization between the same lowest-momentum left and right magnons [black dashed curve on the lower panel in Fig. 7(d)]. These two modes are characterized by the same resonance field [Fig. 7(a)] due to the absence of coupling strength between magnons. This is manifested by zero amplitude for both modes at $z/d = 1/2$. The symmetry in amplitudes of magnetization precession across the thickness leads to the maximum in the intensity for the mode $n = 1$, while for $n = 2$ the intensity is zero $I = 0$ [Fig. 7(b)]. The antisymmetric distribution of amplitudes and zero intensity would require an asymmetric rf field h_{rf} to detect such a mode. The next pair of modes $n = 3$ and $n = 4$ [the red solid and dashed curves on the lower panel in Fig. 7(d)] corresponds to the acoustic and optic hybridization between the second-lowest-momentum of the left and right magnons. A small difference in amplitudes of magnetization precession $\Delta m = 0.14$ arb. at $z/d = 1/2$ for these two modes indicates that the coupling strength between these magnons is not zero. The presence of the coupling strength results in a small difference between resonance fields of these modes $\Delta\mu_0 H_r = 0.7 \text{ mT}$ [Fig. 7(a)]. The symmetry of the amplitudes

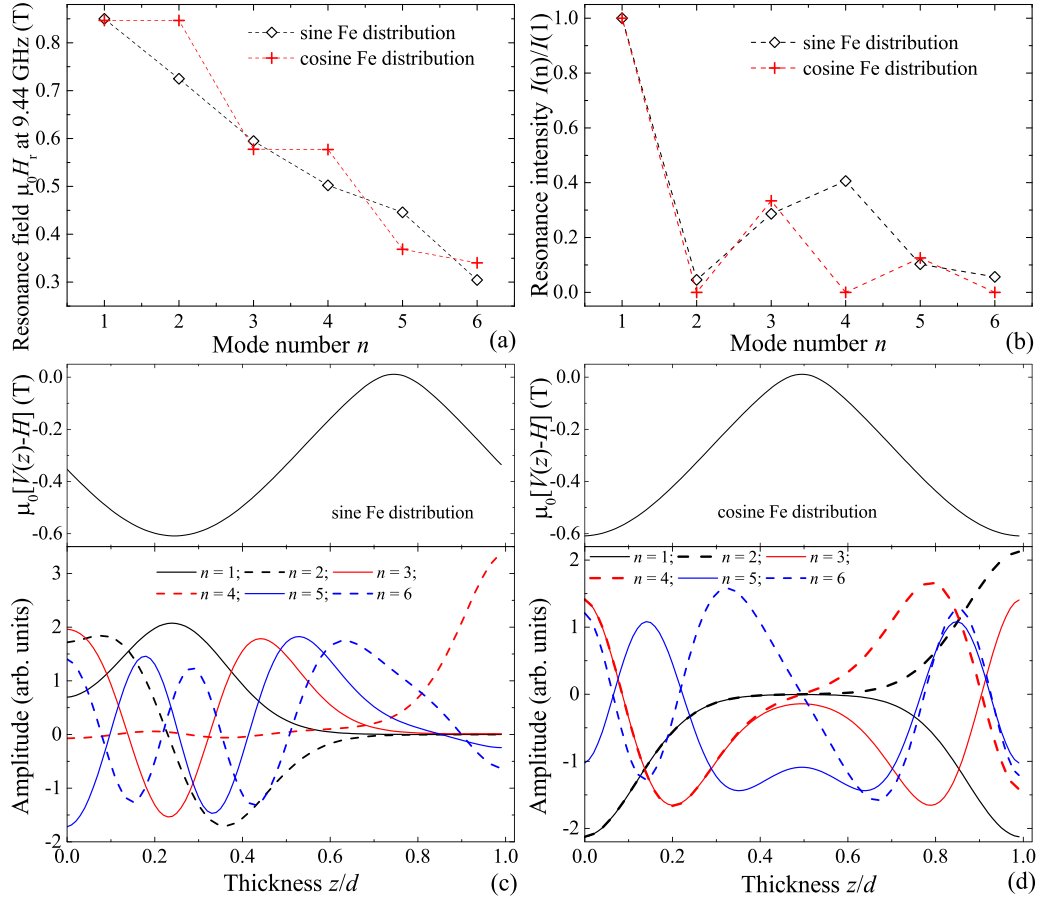


FIG. 7. (a) Dependencies of resonance fields on the mode number $\mu_0 H_r(n)$ at $f = 9.44$ GHz. (b) Normalized dependencies of resonance intensities on the mode numbers $I(n)/I(1)$. (c) Upper panel: Potential $V(z) - H$ [see Eq. (2)] in the case of sine distribution of Fe. Lower panel: Dependencies of amplitudes of magnetization precession across the thickness of the film with sine distribution of Fe for different modes n . (d) Upper panel: Potential $V(z) - H$ [see Eq. (2)] in the case of cosine distribution of Fe. Lower panel: Dependencies of amplitudes of magnetization precession across the thickness of the film with cosine distribution of Fe for different modes n .

of magnetization precession across the thickness leads to the dynamic susceptibility of the acoustic $n = 3$ mode $I \approx 0.3$, while for the optic $n = 4$ mode the intensity $I = 0$ [Fig. 7(b)]. The last pair of presented modes $n = 5$ and $n = 6$ [the blue solid and dashed curves in the lower panel in Fig. 7(d)] corresponds to the acoustic and optic hybridization between the higher-momentum left and right magnons. A significant difference in the amplitudes of magnetization precession $\Delta m = 1.09$ arb. at $z/d = 1/2$ for these two modes indicates sizable coupling strength between these magnons and results in a larger difference between resonance fields $\Delta \mu_0 H_r = 28.5$ mT of these modes [Fig. 7(a)]. The resonance intensity of the acoustic $n = 5$ mode is $I \approx 0.1$, while for the optic mode $n = 6$ the intensity $I = 0$ [Fig. 7(b)].

Overall, these differences in resonance behavior of films with identical maximum, minimum, and average Fe content highlight the potential of ferromagnetic thin films with nonuniform composition for engineering a desired spin-wave spectrum, which can be useful in high-frequency or low-field magnonic operations. In addition, these calculations suggest that ferromagnetic films with nonuniform composition may

become a playground for studying systems with intrinsic magnon-magnon hybridization.

IV. CONCLUSION

Summarizing, we studied magnetic resonance phenomenon in ferromagnetic thin films with engineered nonuniform composition. The Pd-Fe thin film with linear distribution of Fe content across the thickness was used as the model material. Anomalous perpendicular standing spin waves were observed using cavity magnetic resonance spectroscopy and VNA-FMR spectroscopy. Numerical analysis of the resonance conditions using the collective dynamic equation yielded the exchange stiffness constant for the diluted Pd-Fe alloy $D = 2A/\mu_0 M_s = 15$ T \cdot nm² and the ratio of the effective magnetization to the saturation magnetization $M_{\text{eff}}/M_s = 1.16$. As a demonstration, perpendicular standing spin waves were considered numerically in Pd-Fe films with sine and cosine distributions of Fe content. This work suggests that, in comparison to other methods of exploitation of spin waves, the engineering of thin films with a nonuniform

composition across the thickness can become a versatile tool for designing a magnonic media with a desired spectrum, which can be used for high-frequency or low-field magnonic operations. Also, such structures may become a playground for studying intrinsic magnon-magnon hybridization.

ACKNOWLEDGMENTS

The authors acknowledge Dr. V. S. Stolyarov for fruitful discussions. This work was supported by the Russian Science Foundation (Project No. 22-22-00629).

- [1] V. V. Kruglyak, S. O. Demokritov, and D. Grundler, *J. Phys. D* **43**, 264001 (2010).
- [2] A. A. Serga, A. V. Chumak, and B. Hillebrands, *J. Phys. D* **43**, 264002 (2010).
- [3] B. Lenk, H. Ulrichs, F. Garbs, and M. Münzenberg, *Phys. Rep.* **507**, 107 (2011).
- [4] A. V. Chumak, V. I. Vasyuchka, A. A. Serga, and B. Hillebrands, *Nat. Phys.* **11**, 453 (2015).
- [5] G. Csaba, A. Papp, and W. Porod, *Phys. Lett. A* **381**, 1471 (2017).
- [6] A. Barman, G. Gubbiotti, S. Ladak, A. O. Adeyeye, M. Krawczyk, J. Gräfe, C. Adelman, S. Cotofana, A. Naeemi, V. I. Vasyuchka *et al.*, The 2021 magnonics roadmap, *J. Phys.: Condens. Matter* **33**, 413001 (2021).
- [7] A. V. Chumak, P. Kabos, M. Wu, C. Abert, C. Adelman, A. Adeyeye, J. Åkerman, F. G. Aliev, A. Anane, A. Awad *et al.*, Roadmap on spin-wave computing, *IEEE Trans. Magn.* **58**, 0800172 (2022).
- [8] P. Pirro, V. Vasyuchka, A. Serga, and B. Hillebrands, *Nat. Rev. Mater.* **6**, 1114 (2021).
- [9] P. Wessels, A. Vogel, J.-N. TÖdt, M. Wieland, G. Meier, and M. Drescher, *Sci. Rep.* **6**, 22117 (2016).
- [10] A. V. Chumak, A. A. Serga, and B. Hillebrands, *Nat. Commun.* **5**, 4700 (2014).
- [11] Q. Wang, M. Kewenig, M. Schneider, R. Verba, F. Koh, B. Heinz, M. Geilen, M. Mohseni, B. Lägél, F. Ciubotaru, C. Adelman, C. Dubs, S. D. Cotofana, O. V. Dobrovolskiy, T. Brächer, P. Pirro, and A. V. Chumak, *Nat. Electron.* **3**, 765 (2020).
- [12] S. Klingler, P. Pirro, T. Brächer, B. Leven, B. Hillebrands, and A. V. Chumak, *Appl. Phys. Lett.* **106**, 212406 (2015).
- [13] K. Ganzhorn, S. Klingler, T. Wimmer, S. Geprägs, R. Gross, H. Huebl, and S. T. B. Goennenwein, *Appl. Phys. Lett.* **109**, 022405 (2016).
- [14] A. V. Sadovnikov, A. A. Grachev, S. A. Odintsov, A. A. Martyshkin, V. A. Gubanov, S. E. Sheshukova, and S. A. Nikitov, *JETP Lett.* **108**, 312 (2018).
- [15] A. Papp, W. Porod, and G. Csaba, *Nat. Commun.* **12**, 6422 (2021).
- [16] E. Saitoh, M. Ueda, and H. Miyajima, *Appl. Phys. Lett.* **88**, 182509 (2006).
- [17] Y. Kajiwara, K. Harii, S. Takahashi, J. Ohe, K. Uchida, M. Mizuguchi, H. Umezawa, H. Kawai, K. Ando, K. Takanashi, S. Maekawa, and E. Saitoh, *Nature (London)* **464**, 262 (2010).
- [18] W. Zhang, M. Jungfleisch, W. Jiang, J. Pearson, and A. Hoffmann, *J. Appl. Phys.* **117**, 17C727 (2015).
- [19] P. Vaidya, S. Morley, J. van Tol, Y. Liu, R. Cheng, A. Brataas, D. Lederman, and E. del Barco, *Science* **368**, 160 (2020).
- [20] H. Huebl, C. W. Zollitsch, J. Lotze, F. Hocke, M. Greifenstein, A. Marx, R. Gross, and S. T. B. Goennenwein, *Phys. Rev. Lett.* **111**, 127003 (2013).
- [21] Y. Tabuchi, S. Ishino, T. Ishikawa, R. Yamazaki, K. Usami, and Y. Nakamura, *Phys. Rev. Lett.* **113**, 083603 (2014).
- [22] X. Zhang, C.-L. Zou, L. Jiang, and H. X. Tang, *Phys. Rev. Lett.* **113**, 156401 (2014).
- [23] J. T. Hou and L. Liu, *Phys. Rev. Lett.* **123**, 107702 (2019).
- [24] Y. Li, T. Polakovic, Y.-L. Wang, J. Xu, S. Lendinez, Z. Zhang, J. Ding, T. Khaire, H. Saglam, R. Divan, J. Pearson, W.-K. Kwok, Z. Xiao, V. Novosad, A. Hoffmann, and W. Zhang, *Phys. Rev. Lett.* **123**, 107701 (2019).
- [25] I. A. Golovchanskiy, N. N. Abramov, V. S. Stolyarov, M. Weides, V. V. Ryazanov, A. A. Golubov, A. V. Ustinov, and M. Y. Kupriyanov, *Sci. Adv.* **7**, eabe8638 (2021).
- [26] I. A. Golovchanskiy, N. N. Abramov, V. S. Stolyarov, A. A. Golubov, M. Y. Kupriyanov, V. V. Ryazanov, and A. V. Ustinov, *Phys. Rev. Appl.* **16**, 034029 (2021).
- [27] Y. Tabuchi, S. Ishino, A. Noguchi, T. Ishikawa, R. Yamazaki, K. Usami, and Y. Nakamura, *Science* **349**, 405 (2015).
- [28] D. Lachance-Quirion, S. P. Wolski, Y. Tabuchi, S. Kono, K. Usami, and Y. Nakamura, *Science* **367**, 425 (2020).
- [29] X. Zhang, C.-L. Zou, N. Zhu, F. Marquardt, L. Jiang, and H. X. Tang, *Nat. Commun.* **6**, 8914 (2015).
- [30] R. Hisatomi, A. Osada, Y. Tabuchi, T. Ishikawa, A. Noguchi, R. Yamazaki, K. Usami, and Y. Nakamura, *Phys. Rev. B* **93**, 174427 (2016).
- [31] M. T. Johnson, P. J. H. Bloemen, F. J. A. den Broeder, and J. J. de Vries, *Rep. Prog. Phys.* **59**, 1409 (1996).
- [32] A. Haldar, C. Tian, and A. O. Adeyeye, *Sci. Adv.* **3**, e1700638 (2017).
- [33] I. A. Golovchanskiy, N. N. Abramov, M. Pfirrmann, T. Piskor, J. N. Voss, D. S. Baranov, R. A. Hovhannisyanyan, V. S. Stolyarov, C. Dubs, A. A. Golubov, V. V. Ryazanov, A. V. Ustinov, and M. Weides, *Phys. Rev. Applied* **11**, 044076 (2019).
- [34] Y.-C. Lau, Z. Chi, T. Taniguchi, M. Kawaguchi, G. Shibata, N. Kawamura, M. Suzuki, S. Fukami, A. Fujimori, H. Ohno, and M. Hayashi, *Phys. Rev. Materials* **3**, 104419 (2019).
- [35] S. M. Rezende, A. Azevedo, and R. L. Rodriguez-Suárez, *J. Appl. Phys.* **126**, 151101 (2019).
- [36] D. MacNeill, J. T. Hou, D. R. Klein, P. Zhang, P. Jarillo-Herrero, and L. Liu, *Phys. Rev. Lett.* **123**, 047204 (2019).
- [37] I. A. Golovchanskiy, N. N. Abramov, V. A. Vlasenko, K. Pervakov, I. Shchetinin, P. S. Dzhumayev, O. V. Emelianova, D. S. B. D. S. Kalashnikov, K. B. Polevoy, V. M. Pudalov, and V. S. Stolyarov, [arXiv:2108.03847](https://arxiv.org/abs/2108.03847).
- [38] L.-L. Li, Y.-L. Zhao, X.-X. Zhang, and Y. Sun, *Chin. Phys. Lett.* **35**, 077401 (2018).
- [39] I. A. Golovchanskiy, N. N. Abramov, V. S. Stolyarov, V. I. Chichkov, M. Silaev, I. V. Shchetinin, A. A. Golubov, V. V. Ryazanov, A. V. Ustinov, and M. Yu. Kupriyanov, *Phys. Rev. Appl.* **14**, 024086 (2020).
- [40] I. A. Golovchanskiy, N. N. Abramov, V. S. Stolyarov, V. V. Bol'ginov, V. V. Ryazanov, A. A. Golubov, and A. V. Ustinov, *Adv. Funct. Mater.* **28**, 1802375 (2018).
- [41] C. Kittel, *Phys. Rev.* **110**, 1295 (1958).
- [42] M. H. Seavey and P. E. Tannenwald, *J. Appl. Phys.* **30**, S227 (1959).

- [43] S. Klingler, A. V. Chumak, T. Mewes, B. Khodadadi, C. Mewes, C. D. O. S. B. Hillebrands, and A. Conca, *J. Phys. D: Appl. Phys.* **48**, 015001 (2015).
- [44] H. Yu, O. d'Allivy Kelly, V. Cros, R. Bernard, P. Bortolotti, A. Anane, F. Brandl, F. Heimbach, and D. Grundler, *Nat. Commun.* **7**, 11255 (2016).
- [45] S. Klingler, V. Amin, S. Geprägs, K. Ganzhorn, H. Maier-Flaig, M. Althammer, H. Huebl, R. Gross, R. D. McMichael, M. D. Stiles, S. T. B. Goennenwein, and M. Weiler, *Phys. Rev. Lett.* **120**, 127201 (2018).
- [46] J. Chen, C. Liu, T. Liu, Y. Xiao, K. Xia, G. E. W. Bauer, M. Wu, and H. Yu, *Phys. Rev. Lett.* **120**, 217202 (2018).
- [47] C. Liu, J. Chen, T. Liu, F. Heimbach, H. Yu, Y. Xiao, J. Hu, M. Liu, H. Chang, T. Stueckler, S. Tu, Y. Zhang, Y. Zhang, P. Gao, Z. Liao, D. Yu, K. Xia, N. Lei, W. Zhao, and M. Wu, *Nat. Commun.* **9**, 738 (2018).
- [48] Y. Li, W. Cao, V. P. Amin, Z. Zhang, J. Gibbons, J. Sklenar, J. Pearson, P. M. Haney, M. D. Stiles, W. E. Bailey, V. Novosad, A. Hoffmann, and W. Zhang, *Phys. Rev. Lett.* **124**, 117202 (2020).
- [49] V. E. Demidov, S. Urazhdin, and S. O. Demokritov, *Nat. Mater.* **9**, 984 (2010).
- [50] M. Madami, S. Bonetti, G. Consolo, S. Tacchi, G. Carlotti, G. Gubbiotti, F. B. Mancoff, M. A. Yar, and J. Akerman, *Nat. Nanotechnol.* **6**, 635 (2011).
- [51] S. Urazhdin, V. E. Demidov, H. Ulrichs, T. Kendziorczyk, T. Kuhn, J. Leuthold, G. Wilde, and S. O. Demokritov, *Nat. Nanotechnol.* **9**, 509 (2014).
- [52] O. V. Dobrovolskiy, Q. Wang, D. Y. Vodolazov, B. Budinska, R. Sachser, A. V. Chumak, M. Huth, and A. I. Buzdin, *arXiv:2103.10156*.
- [53] J. Chen, J. Hu, and H. Yu, *ACS Nano* **15**, 4372 (2021).
- [54] A. M. Portis, *Appl. Phys. Lett.* **2**, 69 (1963).
- [55] Y. Sasaki, X. Liu, T. Wojtowicz, and J. K. Furdyna, *J. Superconductivity* **16**, 143 (2003).
- [56] T. G. Rappoport, P. Redlinski, X. Liu, G. Zarand, J. K. Furdyna, and B. Janko, *Phys. Rev. B* **16**, 14 (2004).
- [57] H. Puzskarski, *Prog. Surf. Sci.* **9**, 191 (1979).
- [58] V. Ignatchenko and D. Tsikalov, *J. Magn. Magn. Mater.* **510**, 166643 (2020).
- [59] V. A. Ignatchenko and D. S. Tsikalov, *J. Appl. Phys.* **127**, 123903 (2020).
- [60] C. Büscher, T. Auerswald, E. Scheer, A. Schröder, H. V. Löhneysen, and H. Claus, *Phys. Rev. B* **46**, 983 (1992).
- [61] V. V. Bol'ginov, V. S. Stolyarov, D. S. Sobanin, A. L. Karpovich, and V. V. Ryazanov, *JETP Lett.* **95**, 366 (2012).
- [62] I. V. Vernik, V. V. Bol'ginov, S. V. Bakurskiy, A. A. Golubov, M. Y. Kupriyanov, V. V. Ryazanov, and O. Mukhanov, *IEEE Trans. Appl. Supercond.* **23**, 1701208 (2013).
- [63] L. N. Karelina, V. V. Bol'ginov, S. A. Erkenov, S. V. Egorov, I. A. Golovchanskiy, V. I. Chichkov, A. B. Hamida, and V. V. Ryazanov, *JETP Lett.* **112**, 705 (2020).
- [64] L. N. Karelina, R. A. Hovhannisyanyan, I. A. Golovchanskiy, V. I. Chichkov, A. B. Hamida, V. S. Stolyarov, L. S. Uspenskaya, S. A. Erkenov, V. V. Bol'ginov, and V. V. Ryazanov, *J. Appl. Phys.* **130**, 173901 (2021).
- [65] I. A. Golovchanskiy, V. V. Bol'ginov, N. N. Abramov, V. S. Stolyarov, A. B. Hamida, V. I. Chichkov, D. Roditchev, and V. V. Ryazanov, *J. Appl. Phys.* **120**, 163902 (2016).
- [66] A. Esmaeili, I. V. Yanilkin, A. I. Gumarov, I. R. Vakhitov, B. F. Gabbasov, R. V. Yusupov, D. A. Tatarsky, and L. R. Tagirov, *Science China Materials* **64**, 1246 (2021).
- [67] W. M. Mohammed, I. V. Yanilkin, A. I. Gumarov, A. G. Kiiamov, R. V. Yusupov, and L. R. Tagirov, *Beilstein J. Nanotechnol.* **11**, 807 (2020).
- [68] I. Yanilkin, W. Mohammed, A. Gumarov, A. Kiiamov, R. Yusupov, and L. Tagirov, *Nanomaterials* **11**, 64 (2021).
- [69] M. Ewerlin, B. Pfau, C. Gunther, S. Schaffert, S. Eisebitt, R. Abrudan, and H. Zabel, *J. Phys.: Condens. Matter* **25**, 266001 (2013).
- [70] R. A. Ristau, K. Barmak, L. H. Lewis, K. R. Coffey, and J. K. Howard, *J. Appl. Phys.* **86**, 4527 (1999).
- [71] I. A. Golovchanskiy, S. A. Fedoseev, and A. V. Pan, *J. Phys. D* **46**, 215502 (2013).
- [72] M. H. Kryder, E. C. Gage, T. W. McDaniel, W. A. Challener, R. E. Rottmayer, G. Ju, Y.-T. Hsia, and M. F. Erden, *Proc. IEEE* **96**, 1811 (2008).
- [73] S. D. Bader, *Rev. Mod. Phys.* **78**, 1 (2006).
- [74] P. Ho, R. Evans, R. Chantrell, G. Han, G.-M. Chow, and J. Chen, *J. Appl. Phys.* **117**, 213901 (2015).
- [75] J. Becker, O. Mosendz, D. Weller, A. Kirilyuk, J. C. Maan, P. C. M. Christianen, T. Rasing, and A. Kimel, *Appl. Phys. Lett.* **104**, 152412 (2014).
- [76] I. A. Golovchanskiy, N. N. Abramov, V. S. Stolyarov, O. V. Emelyanova, A. A. Golubov, A. V. Ustinov, and V. V. Ryazanov, *Supercond. Sci. Technol.* **30**, 054005 (2017).
- [77] A. Esmaeili, I. V. Yanilkin, A. I. Gumarov, I. R. Vakhitov, B. F. Gabbasov, A. G. Kiiamov, A. M. Rogov, Y. N. Osin, A. E. Denisov, R. V. Yusupov, and L. R. Tagirov, *Thin Solid Films* **669**, 338 (2019).
- [78] See Supplemental Material at <http://link.aps.org/supplemental/10.1103/PhysRevMaterials.6.064406> for details of synthesis and the characterization of Pd-Fe films.
- [79] I. Neudecker, G. Woltersdorf, B. Heinrich, T. Okuno, G. Gubbiotti, and C. H. Back, *J. Magn. Magn. Mater.* **307**, 148 (2006).
- [80] S. S. Kalarickal, P. Krivosik, M. Wu, C. E. Patton, M. L. Schneider, P. Kabos, T. J. Silva, and J. P. Nibarger, *J. Appl. Phys.* **99**, 093909 (2006).
- [81] A. Esmaeili, I. R. Vakhitov, I. V. Yanilkin, A. I. Gumarov, B. M. Khaliulin, B. F. Gabbasov, M. N. Aliyev, R. V. Yusupov, and L. R. Tagirov, *Appl. Magn. Reson.* **49**, 175 (2018).
- [82] R. K. Wangsness, *Phys. Rev.* **91**, 1085 (1953).
- [83] D. L. Hardison and E. D. Thompson, *Journal de Physique Colloques* **32**, C1-565 (1971).
- [84] N. S. Almeida and D. L. Mills, *Phys. Rev. B* **53**, 12232 (1996).
- [85] M. Kostylev, *J. Appl. Phys.* **106**, 043903 (2009).
- [86] K. J. Kennewell, M. Kostylev, N. Ross, R. Magaraggia, R. L. Stamps, M. Ali, A. A. Stashkevich, D. Greig, and B. J. Hickey, *J. Appl. Phys.* **108**, 073917 (2010).
- [87] R. F. Soohoo, *Phys. Rev.* **131**, 594 (1963).
- [88] C. H. Bajorek and C. H. Wilts, *J. Appl. Phys.* **42**, 4324 (1971).
- [89] G. C. Bailey and C. Vittoria, *Phys. Rev. B* **8**, 3247 (1973).
- [90] R. A. Matula, *J. Phys. Chem. Ref. Data* **8**, 1147 (1979).
- [91] Y. Hsu, J. E. Schmidt, M. Gupta, S. Jen, and L. Berger, *J. Appl. Phys.* **54**, 1887 (1983).
- [92] I. V. Yanilkin, A. I. Gumarov, G. F. Gizzatullina, R. V. Yusupov, and L. R. Tagirov, *Beilstein J. Nanotechnol.* **13**, 334 (2022).